RSC Advances

Cite this: *RSC Advances*, 2012, **2**, 11808–11812

www.rsc.org/advances

PAPER

Photoelectrochemistry of solution processed hematite nanoparticles, nanoparticle-chains and nanorods

Supriya A. Patil,†[a] Dipak V. Shinde,†[a] Eun-kyung Kim,[a] Joong Kee Lee,[b] Rajaram S. Mane[c] and Sung-Hwan Han*[a]

Received 2nd May 2012, Accepted 1st October 2012
DOI: 10.1039/c2ra20828h

We report a coordination chemistry approach for shape-controlled synthesis of α-Fe_2O_3 (hematite) nanostructures. Three distinct morphologies *viz.* nanoparticles, nanoparticle-chains and nanorods were synthesized from inorganic iron precursor sources of nitrate, sulfate and chloride, respectively, in the presence of urea as a pH regulating agent and were characterized by X-ray diffraction, scanning electron microscopy and Raman spectroscopy. The responsible growth mechanism and possible factors controlling the morphologies are explored. Photoelectrochemical cells constructed by utilizing these nanostructures produced stable photocurrents in iodide electrolyte. The nanoparticle-chains morphology of α-Fe_2O_3 revealed the highest photocurrent density of 0.36 mA cm^{-2} at 0 V bias conditions under 1 Sun illumination. The reason for the high performance is investigated with the help of impedance spectroscopy analysis, wherein the electrode composed of nanoparticle-chains affords the lowest charge transfer resistance and thereby the highest photoconversion yield, as compared to those of the nanoparticle and nanorod electrodes.

Introduction

Synthesizing controlled arrays of aligned semiconducting metal oxide nanostructures onto conducting substrates has been extensively studied in recent years due to their potential applications in photovoltaic devices,[1] light emitting diodes,[2] gas sensors[3] and electrode materials for electrochemical batteries.[4] Iron oxide is well known for applications in catalysis, gas sensors, pigments, magnetic recording devices *etc.* The properties of iron oxide depend on the phases, nanostructures and shapes *etc.* Shape-controlled synthesis of iron oxide in micro and nanostructure forms plays an important role in potential technical applications. Different phases of iron oxide such as hematite (α-Fe_2O_3), maghemite (γ-Fe_2O_3), and magnetite (Fe_3O_4) have different special properties. Among them, hematite is one of the most interesting and important metal oxides.[5–8] It is an n-type semiconductor with a direct band gap of 2.2 eV. It can be applied as a sensitizer or as a photocatalyst and has good chemical and photoelectrochemical stability, low cost, and ease of fabrication.[9–11] However, when used as a photoanode in photoelectrochemical cells, hematite shows relatively poor light-to-electrical conversion efficiency[12–14] due to two conflicting properties; a) long photon penetration depth, and b) short hole (minority charge carrier) diffusion length. Due to short hole (minority carriers) diffusion length (2–4 nm), most of the photogenerated carriers recombine even before reaching the semiconductor electrolyte interface. One way to overcome these problems is to geometrically orthogonalize these processes.[15,16] This strategy has been applied by using various iron oxide nanostructures, but with low photoconversion yields.[18,19] Various hematite forms including nanoparticles, nanotubes and cauliflowers have been employed as water oxidation photocatalysts but still with a modest photoconversion yield.[20,21] Understanding the structure–function relationship can be interesting for improving power conversion efficiencies. The number of methods designed for the synthesis of iron oxide nanomaterials with distinct morphologies are high-cost and require high temperature, use of surfactants and complexing agents, *etc.*[22–28] For the scalable production of the desired morphology of iron oxide these methods are not viable.

Herein, we report an environmentally friendly route to synthesize hematite nanoparticles, nanoparticle-chains, and nanorod arrays on fluorine doped tin oxide (FTO) substrates by a chemical method at low temperature without the use of any surfactants or complexing agents. In this method production costs are greatly reduced because of the minimal investment of low thermal energy, typically less than 100 °C, required for such growth, and it does not require the high-maintenance and expensive vacuum pumps and chambers that are associated with

[a]*Inorganic Nanomaterials Laboratory, Department of Chemistry, Hanyang University, Seongdong-gu, 133791 Seoul, Republic of Korea. E-mail: shhan@hanyang.ac.kr; Fax: +82 2 2299-0762; Tel: +82 2-2292-5212*
[b]*Energy Storage Research Centre, Korea Institute of Science and Technology, Hwarangno 14-gil 5, Seongbuk-gu, 136791 Seoul, Republic of Korea*
[c]*Centre for Nanomaterials & Energy Devices, School of Physical Sciences, SRTM University, 431606, Nanded, India*
† These authors contributed equally to this work.

vapor deposition. In addition to the simultaneous growth of numerous films free from hazardous processes, unparalleled scalability using this method can be easily achieved. In general, a coordination chemistry approach based on the coordination strength of different ligands is used to control the morphologies of hematite nanomaterials. The key factors controlling the morphologies are also discussed. Photoelectrochemical characteristics were established and electrochemical impedance spectroscopy was performed to establish the structure–function relation.

Experimental

All reagents used in this experiment were of analytical grade, obtained from Sigma Aldrich and used without further purification. Triply-distilled water was used throughout the experiment. FTO substrates used for deposition were first cleaned in detergent water, acetone and isopropyl alcohol for 10 min each using an ultrasonic bath. Then these substrates were dried in a stream of argon and stored for further use. In a typical synthesis of nanoparticle-chains, nanoparticles and nanorods, 25 ml aqueous solutions of 0.2 M $Fe_2(SO_4)_3$, 0.2 M $Fe(NO_3)_3$ and 0.2 M $FeCl_3$, respectively, were mixed with 0.4 M urea (25 ml) solution, sealed in 50 ml falcon tubes and heated at 90 °C for 12 h. FTO substrates were placed vertically in these tubes with the conducting edge facing towards the solution side. After completion of the reaction, reddish iron oxide–hydroxide films formed on FTO substrates were thoroughly washed with water, dried under a stream of argon and annealed at 500 °C for 30 min to get the desired phase *i.e.* α-Fe_2O_3.

Characterizations

Crystal structures and phases of iron oxide were confirmed using an X-ray diffractometer (Rigaku D/MAX 2500 V, Cu-Kα, λ = 0.15418 nm). The thickness and morphology of electrodes were monitored using a scanning electron microscope (SEM, Hitachi S-4200). In order to measure the solar-to-electric power conversion efficiency, the electrodes with different morphologies were incorporated into thin layer sandwich-type cells with a Pt-coated FTO as the counter electrode using a spacer film (50 μm thick polyester film) and an electrolyte iodolyte AN-50 (iodide based low viscosity electrolyte with 0.5 mM triiodide in acetonitrile.) The Pt-coated counter electrodes were prepared by spreading a drop of 2 mM H_2PtCl_6 in *iso*-propanol onto FTO and heating them to 400 °C for 10 min under ambient air. Cell performance was measured by irradiation with 100 mW cm^{-2} white light (1 Sun) with Air Mass (AM) 0 and 1.5 filters as a solar simulator in the presence of a water filter (450 W xenon lamp, Oriel Instruments). Current density was measured using a Keithley 2400 source meter by defining a definite surface area. Impedance spectra were recorded with an Ivium CompactStat impedance analyzer in the range 0.01 Hz to 1.5 MHz. All spectra were recorded at open circuit conditions under 1 Sun illumination. The data was fitted using Z-view software. The incident photon-to-current conversion efficiency (IPCE) was recorded without bias under illumination with respect to a calibrated Melles-Friot silicon diode and measured by changing the excitation wavelength (photon counting spectrometer, ISS Inc. and Keithley 2400).

Results and discussion

The synthesis method involves the reaction of iron ions with hydroxide ions released *in situ* by hydrolysis of urea. Slow hydrolysis of urea and reaction with different iron precursors might have controlled the morphology of iron oxide, as there were no surfactants or complexing agents used in the present case to control the morphology. The different affinity of ligands to iron ions in the precursor controls the local concentration of iron ions and thus produces different nanoforms. The chemical reactions leading to the formation of α-Fe_2O_3 can be represented as given below.

Hydrolysis of urea can be represented as,

$$NH_2CONH_2 + 3H_2O \rightarrow 2NH_4OH + CO_2 \quad (1)$$

Reactions leading to the formation of iron oxide–hydroxide using different iron precursors:

$$FeCl_3 + 3NH_4OH \rightarrow FeOOH + 3NH_4Cl + H_2O \quad (2)$$

$$Fe(NO_3)_3 + 3NH_4OH \rightarrow FeOOH + 3NH_4NO_3 + H_2O \quad (3)$$

$$Fe_2(SO_4)_3 + 6NH_4OH \rightarrow 2FeOOH + 3(NH_4)_2SO_4 + 2H_2O \quad (4)$$

Annealing of the obtained hydroxide produces the hematite phase.

$$2FeOOH \rightarrow Fe_2O_3 + H_2O \quad (5)$$

The phenomenon can be explained on the basis of Pearson's acid base concept, which says that hard acids prefer to bind with hard bases and *vice versa*. In the present case, Fe^{3+} is a hard acid and prefers to bind with a hard base more strongly than with a soft one. The hardness of the ligands used in these experiments decrease in the order $Cl^- > SO_4^{2-} > NO_3^-$, thus it is clear that Cl^- will bind more strongly to Fe^{3+} and thus less Fe^{3+} will be available for reaction with the *in situ* produced OH^- ions. Surfactants and complexing agents, normally used in the shape controlled synthesis of nanomaterials, play a similar role of controlling the local concentrations of ions available for the reaction, thus producing the desired shape. Our approach is beneficial in the sense that the same role is played by the co-ordinating ligands and thus the method does not need any concentration controlling agent. On the other hand, slow hydrolysis of urea at higher temperatures affords controlled release of hydroxide ions. The two crucial factors mentioned above control the shape of iron oxide. With the numerous co-ordinating ligands available for metal ions, a variety of nanostructures can be synthesized using this approach.

Fig. 1 shows the digital photo-images of the iron oxide films on FTO substrates obtained after air-baking. Uniform and crack-free deposition is confirmed from these images. Fig. 2 represents the SEM images of as-synthesized nanoparticles (Np), nanoparticle-chains (Nc) and nanorods (Nr) at different magnifications. The low magnification image confirms uniform growth on the FTO substrate surface. Nanoparticle-chains of iron oxide is a novel architecture growth obtained here for the first time. The nanoparticle-chains (Fig. 2C and D) are around 2 micron in length and around 40 nm in diameter. Nanoparticles

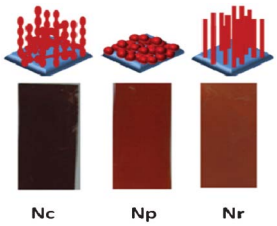

Fig. 1 Cartoon images (top) and digital photo-images of nanoparticle chains (Nc), nanoparticles (Np) and nanorods (Nr) on FTO substrates.

(Fig. 2A and B) are aggregated together (40 nm in size). Fig. 2E indicates that nanorods grow together in a bunch of 7–8 and each individual nanorod is approximately 40 nm in diameter. Fig. 2F indicates that nanorods are not continuous structures but are bifurcated at some places along their length. These various morphologies can have different photoelectrochemical properties depending on their surface area and carrier transportation. X-ray diffraction patterns of all the morphologies are shown in Fig. 3A. All the diffraction patterns match with the hematite phase of iron oxide (JCPDS 88-2346) with the hexagonal unit cell based on anion hcp packing.[12] No obvious impurity phases and peak shift are observed, suggesting a hematite is a single phase of the Nc, Np, and Nr products. Raman spectra of different morphologies are shown in Fig. 3B. Hematite's irreducible vibrational modes at the first Brillouin zone center can be represented as

$$\Gamma_{vib} = 2A_{1g} + 2A_{1u} + 3A_{2g} + 2A_{2u} + 5E_g + 4E_u \quad (6)$$

The acoustic A_{1u} and A_{2u} modes are optically silent, the symmetrical modes are Raman active, and the anti-symmetrical modes are infrared active.[29,30] No modes are both Raman and infra-red active because the hexagonal structure of hematite has an inversion center. These spectra show all peaks corresponding to the hematite phase, and do not contain any peaks associated with other phases of iron oxide. The peaks seen at 229 cm^{-1} and 500 cm^{-1} are assigned to the A_{1g} modes.[17] The remaining five peaks at 249, 295, 302, 414, and 615 cm^{-1} are assigned to the E_g modes.[17]

Photoelectrochemical cells were constructed as explained in the experimental section. Fig. 4A shows the transient photocurrent response of the corresponding electrodes. All the samples

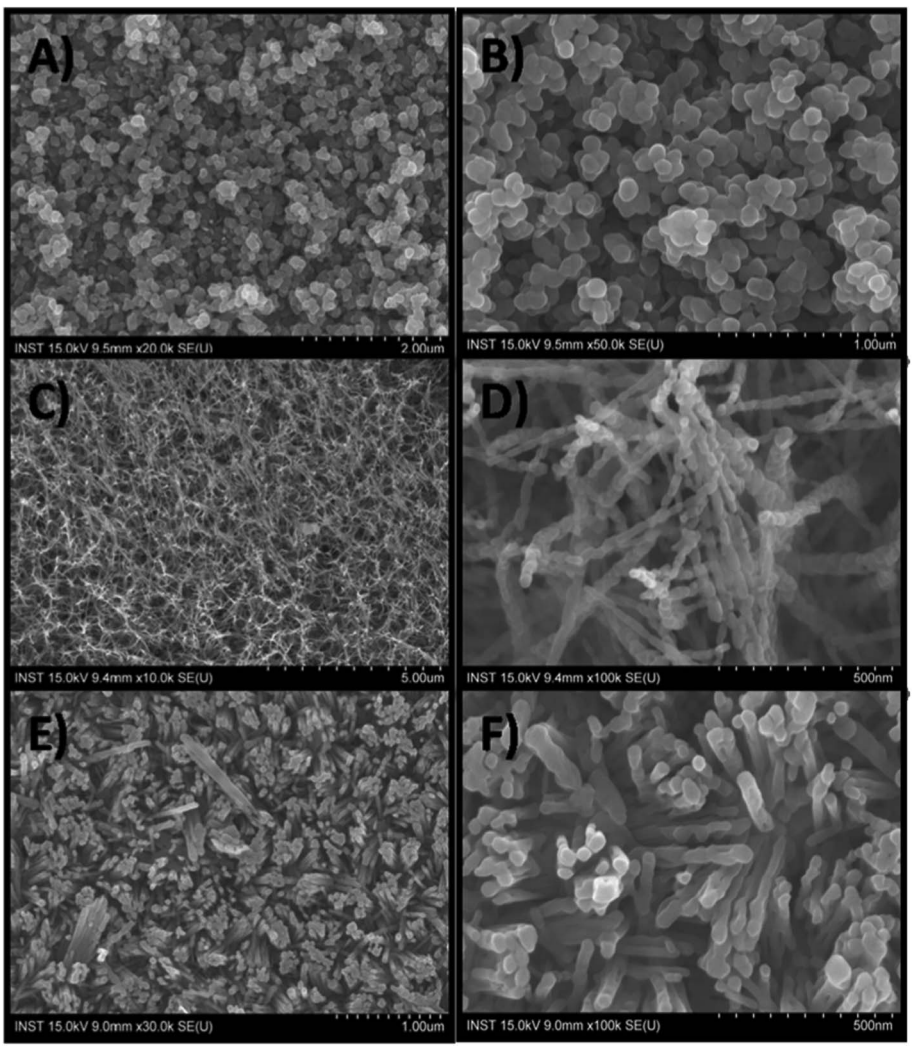

Fig. 2 Scanning electron microscopic images of nanoparticles (A and B), nanoparticle chains (C and D) and nanorods (E and F).

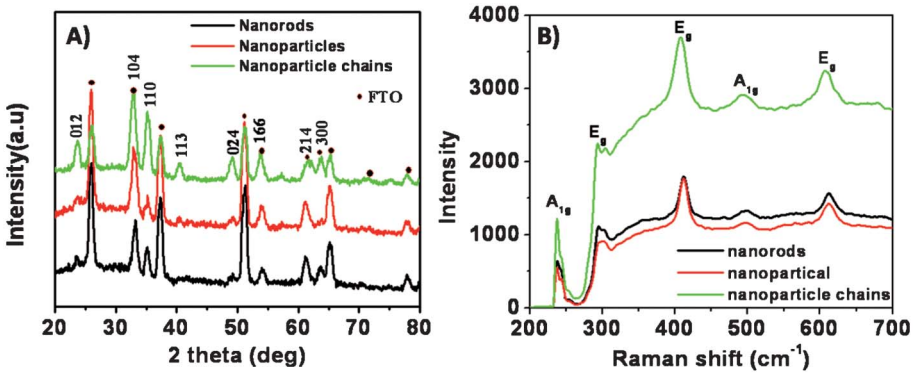

Fig. 3 (A) XRD patterns of iron oxide samples on FTO substrates with different morphologies, (B) Raman spectra of the samples.

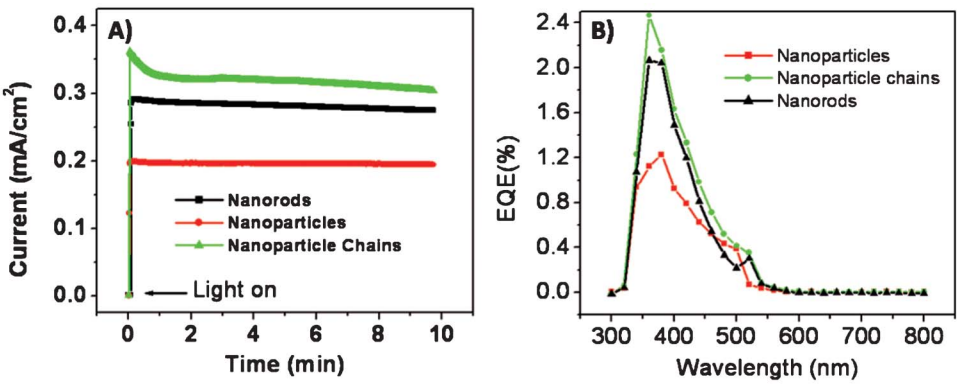

Fig. 4 (A) Transient photocurrent responses of the iron oxide samples with different morphologies at 0 V bias under 1 Sun illumination; the cell area was 0.25 cm^2 and the electrolyte was iodolyte AN-50. (B) Photocurrent action spectra of iron oxide electrodes with different morphologies.

are photoactive and undergo band-gap excitation when illuminated with light, promoting electrons into the conduction band. These electrons then flow through the semiconductor matrix to the anode. Holes are scavenged by I^- present in the redox species while I_3^- ions are reduced back to I^- at the Pt counter electrode. Despite the favorable band-gap for light energy harvesting and high chemical stability in electrolytes, iron oxide shows a smaller power conversion efficiency due to its low minority carrier diffusion length. The Brunauer–Emmett–Teller (BET) surface areas of Np, Nc and Nr samples were found to be 15.99, 65.62 and 13.66 $m^2\ g^{-1}$, respectively. Nanoparticles have a higher surface area than nanorods and thus more effective contact with the electrolyte, however, charge carriers have to clear grain boundaries while moving from one particle to the other, thus there are more chances of a recombination event. On the other hand, nanorods have a smaller effective surface area but charge carriers do not have to pass through the grain boundaries and thus have less chance of recombination. The nanoparticle-chains synthesized in this study can overcome these drawbacks due to their unique structure which, in general, has a high effective surface area and good contact with the electrolyte. Nanoparticle-chain electrodes revealed a highest photocurrent density of 0.36 mA cm^{-2} as compared to those of nanoparticles and nanorod electrodes, probably due to its high effective surface area and superior charge transportation, which might have afforded good contact with the electrolyte and thus easy hole scavenging. This postulate is further supported by impedance measurements, as explained in the following part. The nanorod electrode showed higher photocurrent density than the nanoparticle electrodes. Fig. 4B shows the photocurrent action spectra of the three electrodes. All the electrodes start producing current at 550 nm, which corresponds to a band gap of ~2.26 eV for iron oxide. Nanoparticle-chains showed the highest external quantum efficiency. Electrochemical impedance spectroscopy was performed to evaluate the charge transport properties of the electrodes with different morphologies. The impedance spectra in the present case show one semicircle, which can be attributed to charge transfer resistance at the FTO/Fe_2O_3/electrolyte interface.

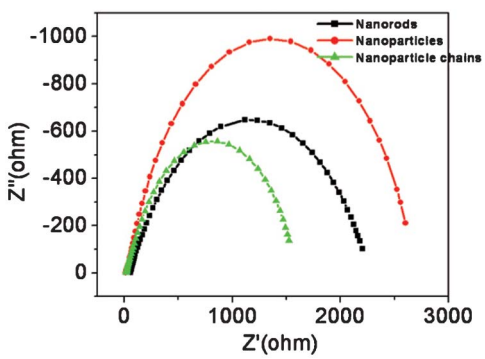

Fig. 5 Electrochemical impedance spectra of iron oxide electrodes recorded at open circuit conditions under 1 Sun illumination. The data were fitted using the Z-view programme.

The system with a lower charge transfer resistance gives a maximum photo-conversion yield. Impedance spectra (Fig. 5) of electrodes with different morphologies suggest that nanoparticle-chains have the lowest charge transfer resistance (R_{ct} = 1512 Ω) as compared to nanoparticles and nanorod electrodes. And thus, it is a pre-eminent system offering high performance in correlation with obtained photocurrents.

Conclusions

In a nutshell, surfactant and complexing agent-free low temperature synthesis of iron oxide in different nanostructures, *viz.* nanoparticle-chains, nanoparticles and nanorods, is presented. Nanoform control is achieved by utilizing the different binding affinities of different ligands to iron metal ions and thus controlling the local concentration of iron ions available for reaction. Photoelectrochemical characteristics showed that nanoparticle chains have better charge transporting properties and offer the highest photocurrent. With a variety of ligands available for co-ordination with the metal ion, a large diversity of nanostructures can be synthesized by our simple and cost effective method.

Acknowledgements

This work was supported by the Korea Research Foundation Grant funded by the Korean Government (MOEHRD, Basic Research Promotion Fund) (KRF-2008-314-D00107). This work was also supported by the KIST internal projects under contracts 2E20980.

References

1 N. K. Shrestha, S. J. Yoon, D. Y. Lee, M. Lee, I. Lim, M. M. Sung, H. Ahn and S. H. Han, *Phys. Status Solidi RRL*, 2011, **5**, 141.
2 H. Guo, J. Zhou and Z. Lin, *Electrochem. Commun.*, 2008, **10**, 146.
3 S. S. Bhande, R. S. Mane, A. V. Ghule and S. H. Han, *Scr. Mater.*, 2011, **65**, 1081.
4 J. Liu, Y. Li, H. Fan, Z. Zhu, J. Jiang, R. Ding, Y. Hu and X. Huang, *Chem. Mater.*, 2009, **22**, 212.
5 R. K. Gupta, K. Ghosh, L. Dong and P.K. Kahol, *Mater. Lett*, 2011, **65.**
6 L. Han and Yu Wei, *Mater. Lett.*, 2012, **70**, 1.
7 M. H. Khedr, K. S. Halim and N. K. Soliman, *Mater. Lett.*, 2009, **63**, 598.
8 K. S. Lin, Z. Wang, S. Chowdhury and A. K. Adhikari, *Thin Solid Films*, 2009, **517**, 5192–5196.
9 *Semiconductor Electrodes*, ed. H. O. Finklea, Elsevier, Amsterdam, 1988, **vol. 55**, p. 43.
10 A. Duret and M. Gratzel, *J. Phys. Chem. B*, 2005, **109**, 17184.
11 T. Lindgren, H. L. Wang, N. Beermann, L. Vayssieres, A. Hagfeldt and S. E. Lindquist, *Sol. Energy Mater. Sol. Cells*, 2002, **71**, 231.
12 I. R. Macdonald, R. F. Howe, S. S. Yarahmadi and K. G. U. Wijayantha, *J. Phys. Chem. Lett.*, 2010, **1**, 2488.
13 M. S. Islam, Y. Kusumoto and Md. A. Mamun, *Mater. Lett.*, 2012, **66**, 165.
14 H. K. Mulmudi, N. Mathews, X. C. Dou, L. F. Xi, S. S. Pramana, Y. M. Lam and S. G. Mhaisalkar, *Electrochem. Commun.*, 2011, **13**, 951.
15 S. W. Boettcher, J. M. Spurgeon, M. C. Putnam, E. L. Warren, D. B. T. Evans, M. D. Kelzenberg, J. R. Maiolo, H. A. Atwater and N. S. Lewis, *Science*, 2010, **327**, 185.
16 A. P. Goodey, S. M. Eichfeld, K. K. Lew, J. M. Redwing and T. E. Mallouk, *J. Am. Chem. Soc.*, 2007, **129**, 12344.
17 I. Chamritski and G. Burns, *J. Phys. Chem. B*, 2005, **109**, 4965.
18 U. Bjorksten, J. Moser and M. Gratzel, *Chem. Mater.*, 1994, **6**, 858.
19 N. Beermann, L. Vayssieres, S. E. Lindquist and A. Hagfeldt, *J. Electrochem. Soc.*, 2000, **147**, 2456.
20 B. M. Klahr, A. B. F. Martinson and T. W. Hamann, *Langmuir*, 2011, **27**, 461.
21 S. Onari, T. Arai and K. Kudo, *Phys. Rev. B: Solid State*, 1977, **16**, 1717.
22 R. A. Rica, M. L. Jimenez and A. V. Delgado, *Soft Matter*, 2012, **8**, 3596.
23 L. H. Han, H. Liu and Y. Wei, *Powder Technol.*, 2011, **207**, 42.
24 N. Pailhé, A. Wattiaux, M. Gaudon and A. Demourgues, *J. Solid State Chem.*, 2008, **181**, 2697.
25 L. E. Barton, K. E. Grant, T. Kosel, A. N. Quicksall and P. A. Maurice, *Environ. Sci. Technol.*, 2011, **45**, 3231.
26 S. Thimmaiah, M. Rajamathi, N. Singh, P. Bera, F. Meldrum, N. Chandrasekhar and R. Seshadri, *J. Mater. Chem.*, 2001, **11**, 3215.
27 M. Mohapatra and S. Anand, *Int. J. Eng. Sci. and Technol.*, 2010, **8**, 127.
28 G. Gnanaprakash, S. Ayyappan, T. Jayakumar, J. Philip and B. Raj, *Nanotechnology*, 2006, **17**, 5851.
29 I. V. Chernyshova and A.S. Madden, *Phys. Chem. Chem. Phys.*, 2007, **9**, 1736.
30 S. P. S. Porto and R. S. Krishnan, *J. Chem. Phys.*, 1967, **47**, 1009.

